applied optics

Beam-pointing drift prediction in pulsed lasers by a probabilistic learning approach

Hui Chang,[1,2] Zhongwei Fan,[1,2,*] Jisi Qiu,[1,2] Wenqi Ge,[1] Haocheng Wang,[1] Ying Yan,[1] Xiongxin Tang,[1] Hongbo Zhang,[1] and Hong Yuan[1,2]

[1]The Academy of Opto-electronics, Chinese Academy of Sciences, No. 9 Dengzhuangnan Road, Haidian, Beijing 100094, China
[2]University of Chinese Academy of Sciences, Beijing 100049, China
*Corresponding author: fanzhongwei@aoe.ac.cn

Received 30 October 2018; revised 17 December 2018; accepted 19 December 2018; posted 21 December 2018 (Doc. ID 348946); published 25 January 2019

In laser systems, it is well known that beam pointing is shifted due to many un-modeled factors, such as vibrations from the hardware platform and air disturbance. In addition, beam-pointing shift also varies with laser sources as well as time, rendering the modeling of shifting errors difficult. While a few works have addressed the problem of predicting shift dynamics, several challenges still remain. Specifically, a generic approach that can be easily applied to different laser systems is highly desired. In contrast to physical modeling approaches, we aim to predict beam-pointing drift using a well-established probabilistic learning approach, i.e., the Gaussian mixture model. By exploiting sampled datapoints (collected from the laser system) comprising time and corresponding shifting errors, the joint distribution of time and shifting error can be estimated. Subsequently, Gaussian mixture regression is employed to predict the shifting error at any query time. The proposed learning scheme is verified in a pulsed laser system (1064 nm, Nd:YAG, 100 Hz), showing that the drift prediction approach achieves remarkable performances.

https://doi.org/10.1364/AO.58.000948

1. INTRODUCTION

High-quality pulsed lasers with frequency 1–1 kHz have been used as major light sources in national high-tech fields such as laser ignition, space debris detection, and ranging. In these fields, beam-pointing stability is a core quality of a pulsed laser [1]. In laser ignition drivers, the stability of beam pointing determines whether the laser can hit targets accurately [2]. In the field of space debris detection and ranging, the stability of beam pointing determines the intensity of echo signals, which affects the precision of orbit determination [3]. However, in a practical sense, pulsed laser beam pointing is prone to unstable drift as a result of complex factors (both internally and externally). Internal factors include temperature distribution, micro motion of laser optical components, and intrinsic random jitters in laser systems. Externally, surrounding variations related to temperature, pressure, and humidity should also be taken into account. All of the aforementioned disturbances will eventually affect performance of beam pointing, making the designing of beam-pointing controllers more difficult. Thus, it is vital to model beam-pointing drift so as to obtain high-performance beam-pointing systems.

So far, many researchers have tried to estimate beam-pointing drift by examining frequency and temporal components. In Ref. [4], the authors analyzed the frequency spectrum of the beam position drift from a spallation neutron source (SNS). Results showed that beam drift often appears with frequency components lower than 1 Hz to 2 Hz, which may help us to select sampling time and control frequency when designing control systems. In addition, the temporal components of beam drift, which may greatly affect performance and parameter tuning of control systems, need to be studied urgently. Fix and Stockl [5] investigated the beam-pointing stability of an optical parametric oscillator (OPO) and used the Allan variance [6] to analyze temporal components of pointing stability. Their results revealed that beam-pointing drift is influenced by white noise ranging from 0.5 s to 10 s, but after 30 s, linear drift becomes significant. In Ref. [7], the authors measured beam wander under varying atmospheric turbulences by changing temperature and wind velocity of the optical turbulence generator chamber. One of their important results proved that the variance of beam drift varied linearly with the temperature gradient. Although those methods can roughly estimate frequency and temporal variation characteristics of beam drift, the model of beam-pointing drift is not established, and the shifting errors cannot be predicted. Due to a variety of un-modeled and time-varying disturbance factors, qualitative modeling of beam-pointing drift in different laser systems by physical modeling approaches is difficult. In contrast to physical modeling approaches that require precise prior knowledge about disturbance factors, a generic method that alleviates any prior disturbances is urgently needed in order to address the problem of modeling and predicting shift dynamics in different laser systems.

Therefore, our work focuses on studying machine learning algorithms in order to provide a new perspective on modeling and predicting beam-pointing drift. Machine learning algorithms can analyze and predict physical models on the basis of pure data while alleviating any prior knowledge. Specifically, in this paper, we consider modeling of the beam-pointing drift phenomenon using the Gaussian mixture model (GMM) [8], which is often used to estimate probability distribution of complex and nonlinear dynamics. Generally, with the joint distribution (obtained by GMM) of relevant variables, Gaussian mixture regression (GMR) [9] is utilized to estimate corresponding condition probability distribution given input signals. Thus, we propose to model the joint distribution of time and drift errors of beam pointing, and subsequently, use GMR to predict drift errors at different time steps. The key advantages of our approach are three-fold: (i) prior disturbance factors are alleviated; (ii) probability distribution of beam-pointing drift dynamics in different laser systems can be estimated; and (iii) shift errors can be predicted at any query time before the laser works, which is highly desired for the design of optimal controllers.

In our experiment, we first capture the beam-pointing drift data from the Nd:YAG, 100 Hz laser at various time steps. Then, based on the training data, we recognize patterns of beam-pointing drift via GMM. In summary, we can use temporal components of the GMM model to predict beam-pointing drift, aiming to improve the performance of beam-pointing control systems.

2. MEASUREMENT SYSTEM

A schematic of the laser source is shown in Fig. 1. For the pulsed laser source, we use a single-longitudinal-mode Q-switched Nd:YAG laser with TEM_{00} mode at wavelength 1064 nm, where the work repetition is 100 Hz and the pulse width is 30 ns. (Note that this laser system was devised by our research group [10].) The gain medium is a 3 mm × 3 mm × 7 mm, Nd^{3+}(1%), Nd:YAG crystal, pumped by fiber-coupled, 2 W, 808 nm laser diodes. With a coupling system consisting of 1 : 2 plano-convex lenses, the pump beam is focused to a beam diameter of about 0.2 mm at the intra-resonator end of the Nd:YAG. The laser cavity consists of a dichroic mirror coated for high transmission at the pump wavelength and high reflectivity at the laser wavelength, and an output coupler coated with 85% reflectivity at the laser wavelength mounted upon a piezoelectric transducer (PZT). An acousto-optic modulator (AOM) with low insertion loss is used to produce Q-switched operation. By inserting the Fabry–Perot (F-P) etalon into the laser cavity, a single-longitudinal-mode laser is obtained. A fraction of the laser is sampled by the photodiode (PD), which provides the signal to match the laser's frequency with the F-P etalon resonance. A driving voltage is fed back to a PZT actuator to keep the single-longitudinal-mode laser operation.

An illustration of the measurement system for the pulsed laser is shown in Fig. 2. An aperture and a filter (coated for high transmission at the laser wavelength and high reflectivity at the pump wavelength) are used to avoid the influence of the pump laser in the measurement. A 4× telescope is introduced to ensure the divergence angle is less. Attenuators are used to protect the scientific CCD. Then the sampling laser beam transmits through the focal lens f ($f = 150$ mm) and is focused on the far-field scientific CCD (LaserCam-HR II, Coherent Inc.) with 1280 × 1024 pixels, 6.5 μm × 6.5 μmla pixel size each, and 400 nm to 1100 nm spectral range.

To run the pulsed laser, start sampling, and compute the centroid drift, a driving and sampling unit is used. Within the pulsed laser running time, a sampling period is set as 20 min as an example to verify the proposed method. (Note that the sampling time is not necessarily 20 min; a longer period is also allowed.)

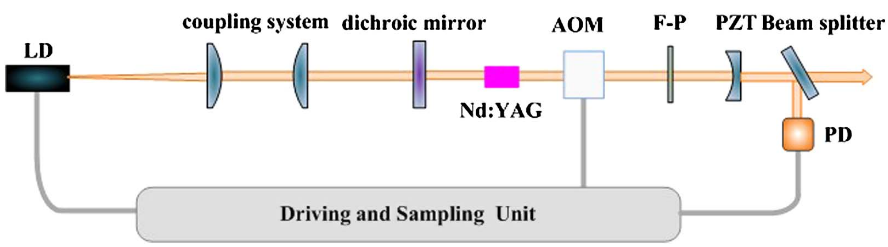

Fig. 1. Overview of the single-longitudinal-mode Q-switched Nd:YAG laser.

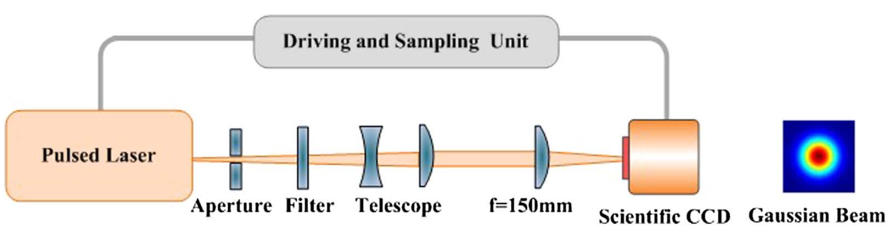

Fig. 2. Overview of measurement system for pulsed lasers.

The sampling frequency of the CCD camera is 5 Hz, and thus a sampling period comprises 6000 samples. The pointing movement of the far-field spot or near-field spot in the x and y axes are calculated by

$$\delta_{\alpha_{x(t)}} = \arctan\frac{\delta x(t)}{f} \approx \frac{\delta x(t)}{f}, \tag{1}$$

$$\delta_{\alpha_{y(t)}} = \arctan\frac{\delta y(t)}{f} \approx \frac{\delta y(t)}{f}, \tag{2}$$

where $\delta_{\alpha_{x(t)}}$ and $\delta_{\alpha_{y(t)}}$ represent translational displacements of the far-field spot in the x and y axes, respectively. From (1) and (2), it can be found that the pointing motions are proportional to translational displacement by the focal length f. So, in our work, we use translational drifts instead.

After a sampling period, training datasets $\mathbf{X}$ and $\mathbf{Y}$ are recorded as

$$\mathbf{X} = \begin{bmatrix} t_1 & \delta x_1 \\ t_2 & \delta x_2 \\ \vdots & \vdots \\ t_N & \delta x_N \end{bmatrix} \quad \text{and} \quad \mathbf{Y} = \begin{bmatrix} t_1 & \delta y_1 \\ t_2 & \delta y_2 \\ \vdots & \vdots \\ t_N & \delta y_N \end{bmatrix}. \tag{3}$$

where $\delta x_i = x_i - x_0$, $\delta y_i = y_i - y_0$ with (x_i, y_i) being the centroid position at t_i and (x_0, y_0) as the expected centroid position. Then, we can use the modeling method GMM/GMR to predict the drift δx in x direction and the drift δy in y direction at time t.

3. MODELING METHODS

With the training datasets $\mathbf{X}$ and $\mathbf{Y}$, we can model the joint probability distribution $\mathcal{P}(t, \delta_x)$ and $\mathcal{P}(t, \delta_y)$ using GMM. Specifically, we have

$$\mathcal{P}(t, \delta_x) \sim \sum_{k=1}^{K} \pi_k \mathcal{N}(\boldsymbol{\mu}_k, \boldsymbol{\Sigma}_k), \tag{4}$$

$$\mathcal{P}(t, \delta_y) \sim \sum_{k=1}^{K} \bar{\pi}_k \mathcal{N}(\bar{\boldsymbol{\mu}}_k, \bar{\boldsymbol{\Sigma}}_k), \tag{5}$$

where π_k, $\boldsymbol{\mu}_k$, and $\boldsymbol{\Sigma}_k$, respectively, represent prior probability, mean, and covariance of the k-th Gaussian component when modeling $\mathcal{P}(t, \delta_x)$. (It is noted that $\sum_{k=1}^{K} \pi_k = \sum_{k=1}^{K} \bar{\pi}_k = 1$ in order to render proper probability distributions).

Similarly, $\bar{\pi}_k$, $\bar{\boldsymbol{\mu}}_k$, and $\bar{\boldsymbol{\Sigma}}_k$, respectively, represent prior probability, mean, and covariance of the k-th Gaussian component when modeling $\mathcal{P}(t, \delta_y)$. Usually, the classical expectation-maximization (EM) algorithm is employed to estimate GMM parameters. The EM algorithm is an iterative algorithm that has two key steps: expectation (E) step and maximization (M) step. When modeling $\mathcal{P}(t, \delta_x)$, in the E step, it tries to calculate the posterior probability $\gamma(i, k)$, which represents the probability of data point (μ_k, Σ_k) belonging to component k. In the M steps, it updates the prior probability, mean, and covariance based on the posterior probability. When modeling $\mathcal{P}(t, \delta_y)$, the procedures are similar. Here is the algorithm: after several iterations of the EM algorithm, the mixture parameters $\lambda = \{\pi_k, \boldsymbol{\mu}_k, \boldsymbol{\Sigma}_k\}_{j=1}^{K}$ and $\bar{\lambda} = \{\bar{\pi}_k, \bar{\boldsymbol{\mu}}_k, \bar{\boldsymbol{\Sigma}}_k\}_{j=1}^{K}$ are obtained. An illustration of the EM algorithm is provided in Algorithm 1. The reader is encouraged to refer to [11] for more details.

Algorithm 1. Expectation Maximization Algorithm

Define K Guassian models $\{k\}_1^K$, N Training set $\{i\}_1^N$
Initialize the estimates μ_k, Σ_k and the mixture weights π_k, $k = 1, \ldots, k$
repeat
  for each k, i **do**
    $\gamma(i, k) := p(t_i, \delta_{x_i} | \mu_k, \Sigma_k)$
    Update the parameters:

$$\pi_k := \frac{1}{m}\sum_{i=1}^{N} \gamma(i, k),$$

$$\mu_k := \frac{\sum_{i=1}^{N} \gamma(i, k)\delta_{x_i}}{\sum_{i=1}^{N} \gamma(i, k)},$$

$$\Sigma_k := \frac{\sum_{i=1}^{N} \gamma(i, k)(\delta_{x_i} - \mu_k)(\delta_{x_i} - \mu_k)^T}{\sum_{i=1}^{N} \gamma(i, k)},$$

  end for
until convergence
Return the final parameter estimates

It is worth pointing out that the Bayesian information criterion (BIC) [12] is often used to choose the number of Gaussian components for GMM, which aims to achieve a compromise between modeling precision and complexity. BIC is defined as

$$\mathrm{BIC}(k) = k \ln(n) - \ln(L(\lambda|z)), \tag{6}$$

where k is the number of components, n is the size of the training set, and $L(\lambda|z)$ is the likelihood of the observed set z given the model parameters λ. $L(\lambda|z)$ is defined as

$$L(\lambda|z) = \sum_{i=1}^{n} \log\left(\frac{1}{k}\sum_{k=1}^{K} p(z_i|\lambda_k)\right), \tag{7}$$

where $p(z_i|\lambda_k)$ is the posterior probability, which represents the probability of the data point belonging to component k.

Once the joint probability distributions $\mathcal{P}(t, \delta_x)$ and $\mathcal{P}(t, \delta_y)$ are obtained, GMR can be used to determine $\mathcal{P}(\delta_x|t)$ and $\mathcal{P}(\delta_y|t)$. For simplicity of discussion, we take the prediction of $\mathcal{P}(\delta_x|t)$ as an example, while $\mathcal{P}(\delta_y|t)$ can be computed in a similar manner. Let us first write Gaussian components from (4) in expanded form, i.e.,

$$\boldsymbol{\mu}_k = \begin{bmatrix} \mu_{k,t} \\ \mu_{k,\delta x} \end{bmatrix} \quad \text{and} \quad \sum\nolimits_k = \begin{bmatrix} \sigma_{k,tt} & \sigma_{k,t\delta_x} \\ \sigma_{k,\delta_x t} & \sigma_{k,\delta_x\delta_x} \end{bmatrix}. \tag{8}$$

Formally, by using GMR, we have [13–15]

$$\mathcal{P}(\delta x|t) \sim \sum_{k=1}^{K} h_k^x(t)\mathcal{N}(\mu_k^x(t), \sigma_k^x), \tag{9}$$

where

$$h_k^x(t) = \frac{\pi_k \mathcal{N}(t|\mu_{k,t}, \sigma_{k,tt})}{\sum_{i=1}^{K} \pi_i \mathcal{N}(t|\mu_{i,t}, \sigma_{i,tt})}, \tag{10}$$

$$\mu_k^x(t) = \mu_{k,\delta x} + \sigma_{k,\delta_x t}\sigma_{k,tt}^{-1}(t - \mu_{k,t}), \tag{11}$$

$$\sigma_k^x = \sigma_{k,\delta_x\delta_x} - \sigma_{k,\delta_x t}\sigma_{k,tt}^{-1}\sigma_{k,t\delta_x}. \tag{12}$$

Thus, for any query time t^*, we can estimate the predicted horizontal movement of spot δx^* from (9). Similarly, the vertical movement of spot δy^* can also be calculated.

4. EXPERIMENTAL RESULTS

To quantitatively estimate the number of components, we compare the BIC values from 1 to 20 components with four training sets by GMMs as we show in Code 1, Ref. [16]. Results are shown in Fig. 3, and the number with the lowest BIC is five. So in this experiment, we will choose five Gaussian components for GMM.

After estimating the beam position probability density by GMMs as well as trajectory prediction and reconstruction of the beam position movements by GMR as we show in Code 2, Ref. [17], the horizontal and vertical results of four independent sample periods are shown in Figs. 4 and 5. In Figs. 4 and 5, green scatter points locate the horizontal and vertical coordinates of the sampling spots centroid, respectively, red ellipses represent GMMs, and the red curves represent the predicted beam drift trajectory. In Fig. 4, approximately sinusoidal drift of the horizontal direction can be found. In horizontal direction, the maximum is about +0.012 mm and the minimum is about −0.018 mm, where the maximum and minimum of corresponding pointing are about +1.4 μrad and −2.09 μrad, respectively. In Fig. 5, the drift of the vertical direction is an irregular sinusoidal motion with different magnitudes. In vertical direction, the maximum is about +0.004 mm and the minimum is about −0.002 mm, where the maximum and minimum of corresponding pointing are about +0.47 μrad and −0.23 μrad, respectively.

In order to observe the relationship between the four sampling periods, we put the four fitting curves of horizontal and vertical trajectories together. In Fig. 6, we find that horizontal and vertical error distributions in multiple tests are almost consistent. Therefore, it is meaningful to study beam-pointing drift over time.

After modeling the beam-pointing drift by GMM, GMR can be employed to predict the shift errors. In order to illustrate the prediction performance of GMR, we resort to two metrics that are widely used in the machine learning community, i.e., mean squared error (MSE) and mean absolute error (MAE), which are defined as follows:

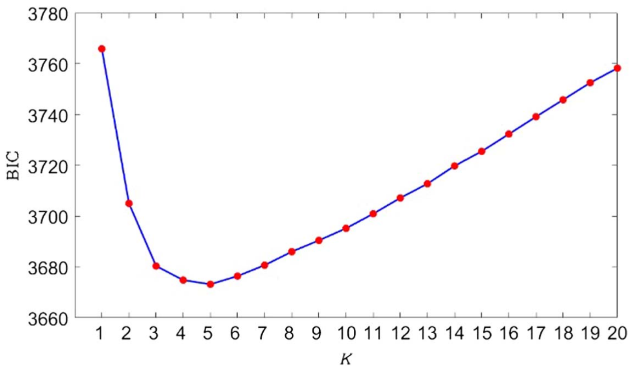

Fig. 3. BIC values with 1 to 20 components.

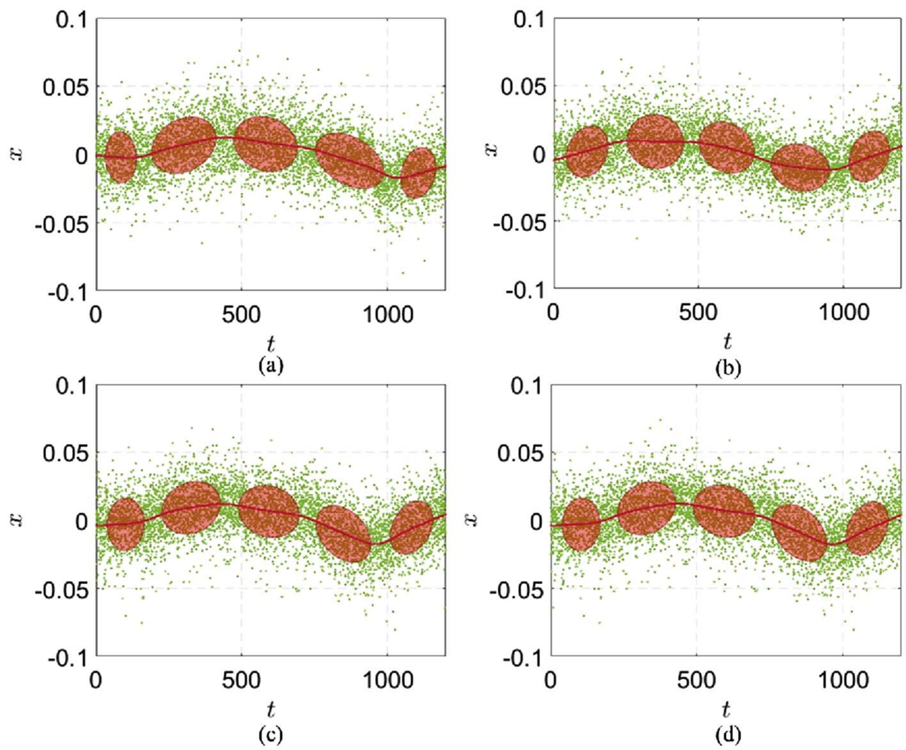

Fig. 4. Time series over 20 min of the horizontal movement of every independent observation. (a) First period. (b) Second period. (c) Third period. (d) Fourth period.

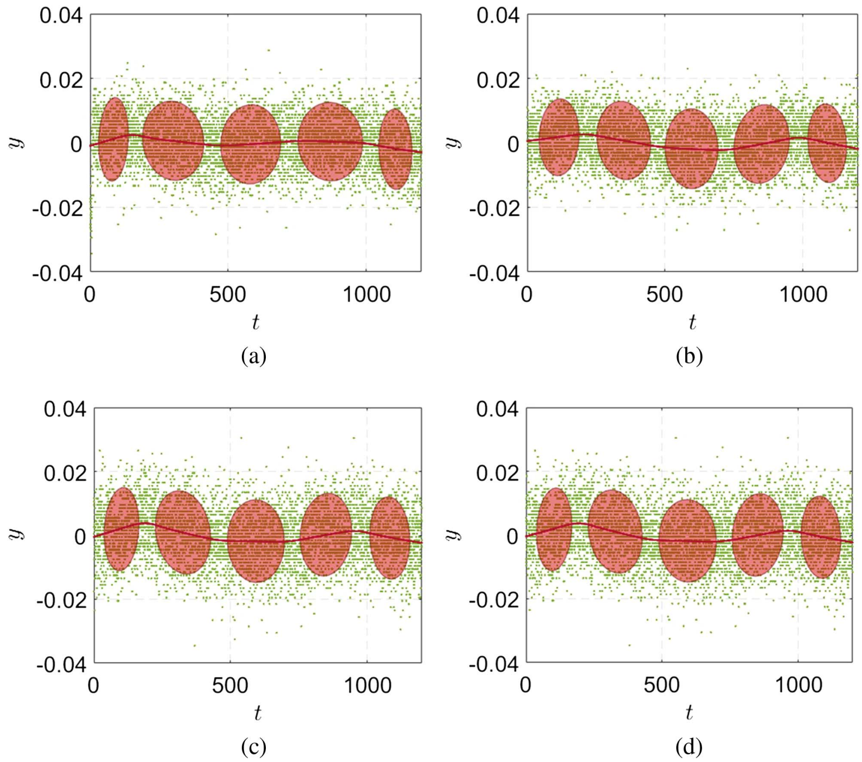

Fig. 5. Time series over 20 min of the vertical movement of every independent observation. (a) First period. (b) Second period. (c) Third period. (d) Fourth period.

$$\mathrm{MSE} = \frac{1}{n}\sum_{i=1}^{n}(y_i - \hat{y}_i)^2, \tag{13}$$

$$\mathrm{MAE} = \frac{\sum_{i=1}^{n}|y_i - \hat{y}_i|}{n}, \tag{14}$$

where y_i and $\hat{y}_i$, respectively, represent the observed and predicted values of the data, and n denotes the number of data points.

Both MSE and MAE are typical metrics in error analysis, as they reflect the average values of predicted errors. MSE measures the average of the squares of errors between the actual observations and predicted values, while MAE measures the average of the magnitudes of errors between the actual and predicted values. Considering that errors could be positive and negative, the square values (used in MSE) and absolute values (MAE) are used to measure the second-order and first-order trend of the magnitude of errors.

We evaluated the prediction capability of GMR by computing the MSE and MAE in four periods. Table 1 shows the MSE and MAE values of the x and y directions in four periods and the total error of the four periods. From both the MSE and MAE values, it can be seen that the prediction of shift errors is reliable with high accuracy.

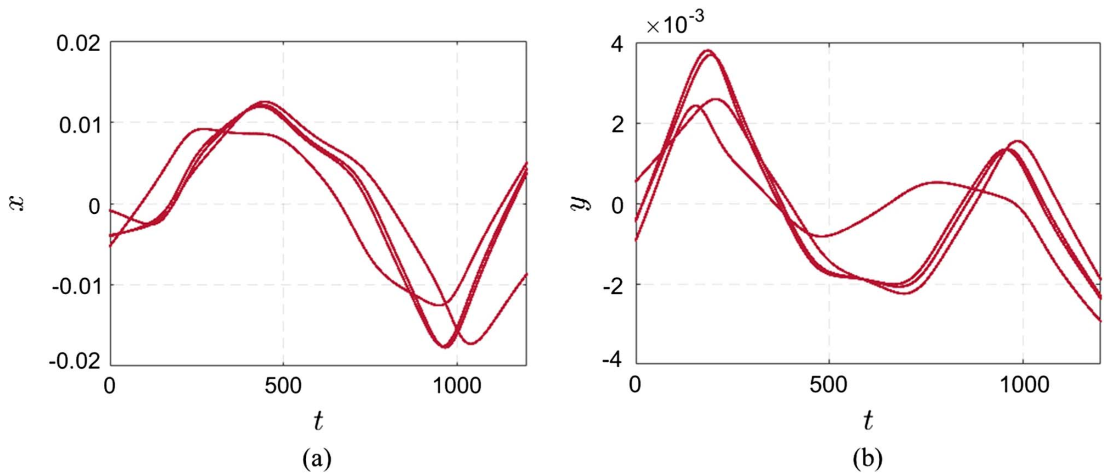

Fig. 6. Predicted errors of four periods in the horizontal direction (a) and vertical direction (b).

Table 1. MSE and MAE Values in Four Periods

	X Direction		*Y* Direction	
Period	MSE[10^{-3}]	MAE	MSE[10^{-3}]	MAE
1	0.2734	0.0128	0.0528	0.0057
2	0.2439	0.0121	0.0475	0.0055
3	0.2663	0.0127	0.0670	0.0065
4	0.2666	0.0127	0.0671	0.0065
Total	0.2626	0.0126	0.0586	0.0061

Table 2. Comparison of Our Method and MA Method

	X Direction		*Y* Direction	
	MSE[10^{-3}]	MAE	MSE[10^{-3}]	MAE
GMR	0.2686	0.0127	0.0685	0.0065
MA	0.3757	0.0154	0.0788	0.0070

Furthermore, we consider the moving average (MA), which is a common method to predict drift errors, as a baseline to illustrate the superiority of our approach. According to the previous drift values, MA is capable of estimating the drift at the next time step. Specifically, MA predicts the drift by using

$$\hat{y}_{n+1} = \frac{1}{n}\sum_{j=1}^{n} y_j, \tag{15}$$

where y_j represents the observed value at previous time steps, and $\hat{y}_{n+1}$ represents the predicted value of the time $n+1$. It is worth emphasizing that MA needs previous drifts to estimate the current drift. In contrast, our method can predict drifts at any query time according to the drift distribution before experiments. Given the four period observations in the starting 5 min, Table 2 represents the beam-pointing drift prediction performances from 5 min to 10 min by using our method and MA method. In Table 2, it is seen that the lower value of MSE and MAE is shown for the GMR model when compared to the MA method. Thus, we can conclude that our approach has better performance and provides more accurate beam-pointing drift prediction.

5. CONCLUSION

Laser beam pointing may drift due to mechanical vibrations, temperature drift, and other unknown noise. The complex disturbance makes it harder to design a beam-pointing control system. Few studies have mentioned beam-pointing prediction methods. In our work, a method based on GMM/GMR to analyze the probability model of beam-pointing drift and retrieve the trajectories was studied in order to predict beam-pointing drift of a pulsed laser. The beam pointing drift of a pulsed, 1064 nm, Nd:YAG laser was analyzed in detail. The beam position movement data of the four independently observed running sets were sampled. Approximated motion profiles in the two directions were found and could be used in a new period for predicting the pointing drift. Comparing the horizontal and vertical error distributions of four sampling periods, the error distributions varying in time of the two directions were almost consistent. With beam-pointing trajectories, the control strategy can be designed more effectively, and more control accuracy will be achieved. In future work, we will design a beam-pointing control system based on beam-pointing trajectories by GMM/GMR.

Funding. National Key Research and Development Program of China (2017YFB1104602).

REFERENCES

1. K. Zhang, F. Chen, G. Yang, D. Li, and J. Guo, "Precise measurement for beam pointing stability of high power repetition rate TEA CO_2 laser," Optik **131**, 892–898 (2017).
2. L. Ding, S. Li, Z. Lu, Y. Wang, C. Zhu, Y. Chen, P. Du, C. Cui, L. Zhou, and H. Yuan, "Analysis of the beam-pointing stability in the high power laser system," Optik **127**, 6056–6061 (2016).
3. A. Palosz, "Higher order sliding mode control of laser pointing for orbital debris mitigation," Ph.D. thesis (The University of Alabama in Huntsville, 2013).
4. R. A. Hardin, Y. Liu, C. Long, A. Aleksandrov, and W. Blokland, "Active beam position stabilization of pulsed lasers for long-distance ion profile diagnostics at the spallation neutron source (SNS)," Opt. Express **19**, 2874–2885 (2011).
5. A. Fix and C. Stockl, "Investigations on the beam pointing stability of a pulsed optical parametric oscillator," Opt. Express **21**, 10720–10730 (2013).
6. D. W. Allan, "Statistics of atomic frequency standards," Proc. IEEE **54**, 221–230 (1966).
7. H. Kaushal, V. Kumar, A. Dutta, H. Aennam, V. Jain, S. Kar, and J. Joseph, "Experimental study on beam wander under varying atmospheric turbulence conditions," IEEE Photon. Technol. Lett. **23**, 1691–1693 (2011).
8. D. Reynolds, "Gaussian mixture models," in *Encyclopedia of Biometrics* (Springer, 2015), pp. 827–832.
9. H. G. Sung, "Gaussian mixture regression and classification," Ph.D. thesis (Rice University, 2004).
10. J. Qiu, X. Tang, Z. Fan, and H. Wang, "200 Hz repetition frequency joule-level high beam quality Nd: YAG nanosecond laser," Opt. Commun. **368**, 68–72 (2016).
11. C. M. Bishop, *Pattern Recognition and Machine Learning* (Springer, 2006).
12. G. Schwarz, "Estimating the dimension of a model," Ann. Stat. **6**, 461–464 (1978).
13. D. A. Cohn, Z. Ghahramani, and M. I. Jordan, "Active learning with statistical models," J. Artificial Intelligence Res. **4**, 129–145 (1996).
14. S. Calinon, "A tutorial on task-parameterized movement learning and retrieval," Intell. Serv. Robot. **9**, 1–29 (2016).
15. Y. Huang, L. Rozo, J. Silvério, and D. G. Caldwell, "Kernelized movement primitives," arXiv:1708.08638 (2017).
16. H. Chang, "selectBIC demo.rar," figshare, 2018, https://doi.org/10.6084/m9.figshare.7472072, retrieved 21 December 2018.
17. H. Chang, "gmrgmm demo.rar," figshare, 2018, https://doi.org/10.6084/m9.figshare.7472069, retrieved 21 December 2018.